

Internal Gravity Wave Breaking in White Dwarf Binaries

Yubo Su,¹ Daniel Lecoanet,² Dong Lai,¹

¹ *Cornell Center for Astrophysics and Planetary Science, Department of Astronomy, Cornell University, Ithaca, NY 14853, USA*

² *Princeton Center for Theoretical Science, Princeton University, Princeton, NJ 08544, USA*

Accepted XXX. Received YYY; in original form ZZZ

ABSTRACT

In white dwarf binaries tidal torques are expected to raise a train of internal gravity waves in the white dwarf interior. These outward-propagating waves can then grow to be nonlinear and break via hydrodynamical instabilities, transferring energy and angular momentum from the binary orbit to the white dwarf. We perform 2D numerical simulations of nonlinear wave breaking of outwards-propagating internal gravity waves in an incompressible, isothermal atmosphere with an exponentially decaying density stratification. We find that tidal synchronization, after an initial transient phase, proceeds inwards from the surface in thin layers. We argue the thickness of these layers is limited by the Kelvin-Helmholtz Instability. We provide simple analytical formulae for the location and thickness of tidal synchronization over time that are in good agreement with our simulations.

Key words: white dwarfs – hydrodynamics – binaries:close – waves

1 INTRODUCTION

Compact white dwarf (WD) binary systems, with orbital periods in the range of minutes to hours, are important for a range of astrophysical problems. They are the most important sources of gravitational waves (GWs) for the Laser Interferometric Space Antenna (LISA) (Nelemans 2009). They are also thought to produce interesting optical transients such as underluminous supernovae (Perets et al. 2010), Ca-rich fast transients (García-Berro et al. 2017), and tidal novae (Fuller & Lai 2012b). Most importantly, they have been proposed as the likely progenitors of type Ia supernovae (e.g. (Iben Jr & Tutukov 1984; Webbink 1984) or more recently (Gilfanov & Bogdán 2010; Maoz et al. 2010)). While presently only a few tens of compact WD binaries are known (Korol et al. 2017), *Gaia* (currently gathering data) is expected to expand the catalog to a few hundreds (Korol et al. 2017) (results based on *Gaia*’s second data release have already begun to appear (Shen et al. 2018; Kilic et al. 2018)), and the Large Synoptic Survey Telescope (LSST, first light scheduled for 2020) will likely detect a few thousand more (Korol et al. 2017). These observations will significantly advance the understanding of WD binaries and their evolution. My proposed theoretical and computational research is well-timed to take advantage of these new advances.

In spite of the broad importance of WD binaries, the evolution of these systems prior to their final mergers is not well understood. Much of this uncertainty comes from our imprecise understanding of tidal interactions, which play an important role during a compact WD binary’s inspiral (Fuller & Lai 2012a). Previous studies have shown that these interactions manifest as tidal excitation of internal gravity waves (IGW), waves in the WD fluid restored by the buoyancy force due to density stratification (Fuller & Lai 2011). As these waves propagate outwards towards the WD surface, they grow

in amplitude until they break, as do ocean waves on a shore, and transfer both energy and angular momentum from the binary orbit to the outer envelope of the WD (Fuller & Lai 2011, 2012a).

Previous works have found that the dissipation of IGW can generate significantly more energy than thermal radiation from the isolated WD surface and is thus a major contributor to the WD energy budget (Fuller & Lai 2012a, 2013). However, these works parameterized the wave breaking process in an ad hoc manner. The details of dissipation, namely the location and spatial extent of the wave breaking, affect the observable outcome: dissipation near the surface of the WD can be efficiently radiated away and simply brightens the WD, while dissipation deep in the WD envelope causes an energy buildup that results in energetic flares (Fuller & Lai 2012b). Works in other fields based on numerical simulations show that strongly nonlinear wave breaking behaves differently than predictions based in linear and weakly nonlinear theory (Winters & D’Asaro 1994; Barker & Ogilvie 2010). Such fully nonlinear numerical simulations have not been performed for WDs.

In Section 2, we will describe the system of equations we will use to analyze IGW breaking. In Section 3, we discuss relevant analytical results. In Section 5 we present the results of numerical simulations. Finally, in Section 6 we discuss the results of the preceding section.

2 PROBLEM DESCRIPTION

We consider a two-dimensional incompressible, isothermal fluid, representative of degenerate matter in WDs. We neglect temperature variations and assume a barotropic equation of state as a first approximation. As we are interested in dynamics far from the center of the WD, we approximate the gravitational field

as uniform. We model the background density stratification as $\rho_0(x, z) = \rho_0(z) = \rho_0(z=0)e^{-z/H}$ for some reference density $\rho_0(z=0) = \rho_0(z)|_{z=0}$.

The Euler equations for an incompressible, barotropic fluid in a uniform gravitational field are

$$\vec{\nabla} \cdot \vec{u} = 0, \quad (1a)$$

$$\frac{D\rho}{Dt} = 0, \quad (1b)$$

$$\frac{D\vec{u}}{Dt} + \frac{\vec{\nabla}P}{\rho} + g\hat{z} = 0. \quad (1c)$$

$\frac{D}{Dt} = \frac{\partial}{\partial t} + (\vec{u} \cdot \vec{\nabla})$ is the Lagrangian or material derivative. \vec{u}, ρ, P denote the velocity field, density and pressure respectively. We denote $-g\hat{z}$ constant gravitational acceleration. Note that at hydrostatic equilibrium $\frac{\partial}{\partial t} = 0$ we have $\vec{\nabla}P_0 = -\rho_0 g\hat{z}$ and so $P_0 = \rho_0 gH$. A shear flow $u_x(x, z, t) = u_x(z)$ is permitted in hydrostatic equilibrium, but we will initially consider no shear flow in equilibrium.

In practice, it is convenient to introduce coordinate $\Upsilon = \ln \frac{\rho}{\rho_0}$. This both identically enforces $\rho > 0$ and avoids numerical issues if ρ is small. We also define reduced pressure $P = \frac{P}{\rho}$. Then, we may rewrite the second two equations of Equation 1 as

$$\frac{D\Upsilon}{Dt} + u_z \frac{\partial \ln \rho_0}{\partial z} = 0, \quad (2a)$$

$$\frac{D\vec{u}}{Dt} + \vec{\nabla}P + P\vec{\nabla}\Upsilon + g\hat{z} = 0. \quad (2b)$$

Note that in the new coordinates, hydrostatic equilibrium corresponds to $\Upsilon_0 = 1, P_0 = gH$.

3 INTERNAL GRAVITY WAVES: THEORY

3.1 Analytical Properties: Linear

In the small perturbation limit, where flow velocities are small compared to the characteristic space and time scales $\frac{\partial}{\partial t} \gg \vec{u} \cdot \vec{\nabla}$, we may linearize Equation 2. We ignore the advective components of the material derivative and consider small deviations $\Upsilon_1 = \Upsilon - \Upsilon_0, P_1 = P - P_0$ about hydrostatic equilibrium:

$$\vec{\nabla} \cdot \vec{u} = 0, \quad (3a)$$

$$\frac{\partial \Upsilon_1}{\partial t} - \frac{u_z}{H} = 0, \quad (3b)$$

$$\frac{\partial \vec{u}}{\partial t} + \vec{\nabla}P_1 + (1 + \Upsilon_1)g\hat{z} = 0. \quad (3c)$$

This can be solved to obtain solutions up to undetermined amplitude A the well-known result (Drazin 1977; Dosser & Sutherland 2011b):

$$u_z(x, z, t) = Ae^{z/2H} e^{i(k_{0x}x + k_{0z}z - \omega_0 t)}, \quad (4a)$$

$$\omega_0^2 = \frac{N^2 k_{0x}^2}{k_{0x}^2 + k_{0z}^2 + \frac{1}{4H^2}}, \quad (4b)$$

where

$$N^2 \equiv g^2 \left(\frac{d\rho}{dP} - \frac{\partial \rho}{\partial P} \Big|_{ad} \right) = \frac{g}{H}, \quad (5)$$

the Brunt-Väisälä frequency is constant

In the weak stratification limit $k_{0z}H \gg 1$, the solution exhibits the following characteristics:

- The amplitude of the wave grows like $e^{z/2H}$. Thus, the linear approximation is violated for sufficiently large z .

- The phase and group velocities can be computed respectively:

$$\vec{c}_{ph} = \left(\frac{\hat{x}}{k_{0x}} + \frac{\hat{z}}{k_{0z}} \right) \omega, \quad (6)$$

$$\begin{aligned} \vec{c}_g &= \frac{N \left(k_{0x} k_{0z} \hat{x} - \left(k_{0z}^2 + \frac{1}{4H^2} \right) \hat{z} \right)}{\left(k_{0x}^2 + k_{0z}^2 + \frac{1}{4H^2} \right)^{3/2}} \\ &\approx \frac{\omega k_{0z}}{|\vec{k}_0|^{3/2}} (k_{0x} \hat{x} - k_{0z} \hat{z}). \end{aligned} \quad (7)$$

We recover the usual result $\vec{c}_{ph} \cdot \vec{c}_g = 0$ (e.g. (Drazin 1977; Dosser & Sutherland 2011a)). Note that an IGW transporting energy and momentum upwards $c_{g,z} > 0$ has $k_{0z} < 0$.

- The time-averaged total x -momentum flux in the \hat{z} direction can be computed. Since the linear solution is separable as $f(x, z, t) = f(z)e^{i(k_{0x}x - \omega_0 t)}$, x averaging and time averaging are equivalent, so we may write

$$S \equiv \langle \rho u_x u_z \rangle_x \equiv \frac{1}{L_x} \int_0^{L_x} \rho u_x u_z dx, \quad (8)$$

$$\approx -\frac{A^2}{2} \rho_0(z=0) \frac{k_{0z}}{k_{0x}}, \quad (9)$$

where $\langle \dots \rangle_x$ denotes x -averaging.

3.2 Wave Generation

To model a continuous IGW wave train excited deep in the WD interior propagating towards the surface, we use a volumetric forcing term to excite IGW near the bottom of the simulation domain¹. Our forcing excites both IGWs propagating upwards, imitating a wave tidally excited deeper in the WD, and downwards, which are damped away by the damping layers described in subsection 4.2.

As not to interfere with the incompressibility constraint, we force the system on the density equation. This constitutes replacing Equation 2a with

$$\frac{D\Upsilon}{Dt} + u_z \frac{\partial \ln \rho_0}{\partial z} = F e^{-\frac{(z-z_0)^2}{2\sigma^2}} \cos(k_{0x}x - \omega_0 t). \quad (10)$$

Using a narrow Gaussian profile excites a broad k_z wavenumber spectrum, and only the k_{0z} satisfying dispersion relation Equation 4b for the given $k_{0x}, \omega_0(k_{0x}, k_{0z})$ will propagate.

In the linearized system, the effect of this forcing can be solved analytically up to good accuracy: we first approximate the driving term using $e^{-\frac{(z-z_0)^2}{2\sigma^2}} \approx \sqrt{2\pi\sigma^2} \delta(z - z_0)$, the $\sigma \rightarrow 0$ limit². This system is solved exactly by matching the two homogeneous solutions above and below z_0 . We may then approximately relax the solution to nonzero σ : an extra factor of $e^{-\frac{(k_{0z}\sigma)^2}{2}}$ arises compared to the δ -function solution (evaluating the Fourier Transform of $e^{-\frac{(z-z_0)^2}{2\sigma^2}}$

¹ Interfacial forcing at the bottom boundary incurs strong stability limits, as we use a Chebyshev polynomial basis along the z axis in our spectral method which has very small grid spacing at the boundaries.

² In practice, σ must be large enough to be numerically resolved by the spectral code.

at $k_z = k_{0z}$), and we obtain

$$u_{1z}(x, z, t) = \frac{F g k_{0x}^2}{\omega_0^2} \frac{1}{2i k_{0z}} \frac{e^{-\frac{(k_{0x}\sigma)^2}{2}}}{\sqrt{2\pi\sigma^2}} \times \begin{cases} e^{\frac{z-z_0}{2H}} e^{i(k_{0x}x + k_{0z}(z-z_0) - \omega_0 t + \frac{1}{2k_{0z}H})} & z > z_0 \\ e^{\frac{z-z_0}{2H}} e^{i(k_{0x}x - k_{0z}(z-z_0) - \omega_0 t + \frac{1}{2k_{0z}H})} & z < z_0 \end{cases}. \quad (11)$$

The $z > z_0$ solution models an upwards-propagating IGW wavetrain inbound on the simulation domain from below. The solution for $u_{1x}(x, z, t)$ can be obtained analytically from Equation 1a.

3.3 Wave Breaking

In developing the results above, we have neglected advective terms $\frac{\partial}{\partial t} \gg \vec{u} \cdot \vec{\nabla}$. However, since $|\vec{u}| \propto e^{z/2H}$, any nonzero amplitude IGW will eventually violate the linearity criterion. This regime is relevant in practice since the IGW may grow to nonlinear amplitudes before it reaches the surface of the WD (Fuller & Lai 2011, 2012a). We can coarsely estimate the height at which this happens by when the Lagrangian displacement $\vec{\xi}$ of a fluid parcel satisfies

$$\vec{\xi} \cdot \vec{k} \gtrsim 1. \quad (12)$$

The general understanding of nonlinear IGW breaking is that the waves' interactions with the mean flow of the fluid transfer horizontal momentum from the waves into the fluid; such a process has been conjectured to be responsible for tidal synchronization in stellar binaries (Zahn 1975; Goldreich & Nicholson 1989) as well as the quasi-biennial oscillation (Lindzen & Holton 1968). The details of this process have been laid out in a few key papers: IGWs are globally unstable to resonant three-wave interactions (Drazin 1977), causing energy transfer out of the IGW to daughter modes. These steeper daughter modes facilitate wave breaking, depositing horizontal momentum in the fluid's mean flow (Klostermeyer 1991). Once the mean flow reaches the horizontal phase velocity of the parent IGW, a critical layer forms at which the frequency of the IGW is Doppler-shifted to zero. The interaction of the parent IGW with the mean flow was first studied in the inviscid, linear regime in (Booker & Bretherton 1967), which found nearly complete absorption. This result was reproduced with nonzero viscosity (Hazel 1967), but weakly nonlinear theory (Brown & Stewartson 1982) and fully nonlinear simulations (Winters & D'Asaro 1994) suggest that nonlinear effects can induce reflection.

An estimate of where these mean flow effects become important can be made using the wave-induced mean flow (Andrews & McIntyre 1976; Dosser & Sutherland 2011b):

$$\langle u_x \rangle = \bar{U}_0 \equiv \frac{1}{L_x} \int u_x dx = \frac{\langle u_x u_x \rangle_x}{c_{g,z}}, \quad (13)$$

where $\langle \dots \rangle_x$ denotes horizontal averaging. Setting $\bar{U}_0 = c_{ph,x}$ the critical layer condition, we recover $\frac{u_x k_x}{\omega} = \xi_x k_x \sim 1$, roughly equivalent to the nonlinearity criterion Equation 12.

4 INTERNAL GRAVITY WAVES: LINEAR NUMERICAL SIMULATION

Towards numerical simulation of IGW breaking, we first verify agreement with linear theory at weak forcing amplitudes. We perform direct numerical simulation using the pseudo-spectral code Dedalus (Burns et al. 2016). In subsection 4.1 we discuss choices

of numerical parameters, in subsection 4.2 we separately discuss use of a damping zone at the top and bottom of the domain, and in subsection 4.3 we present the results of our “linear” simulations, where we solve the full nonlinear fluid equations for weak forcing.

4.1 Numerical Setup

We nondimensionalize by taking $H = N = \rho_0(z = 0) = 1$ in Equation 1.

Denote L_x, L_z to be the physical dimensions of the simulation domain. Our simulation domain is smaller than our full physical domain, so we adopt reflection-suppressing boundary conditions. We use periodic boundary conditions in the x direction and damping layers (described in subsection 4.2) in the z direction to damp perturbations exiting the top and bottom of the domain. We use a Fourier basis in the x direction and either a Chebyshev or Fourier basis in the z direction; our results were robust to either set of basis functions. We varied the number of x, z modes (denoted N_x, N_z respectively), and used 3/2 dealiasing (Boyd 2001).

The time integration uses a split implicit-explicit third-order scheme where certain terms are treated implicitly and the remaining terms are treated explicitly. A third-order, four-stage DIRK-ERK scheme (Ascher et al. 1997) is used with adaptive timesteps computed from advective Courant-Friedrichs-Lewy (CFL) time. Specifically, we use $\Delta t = 0.7 \min(\Delta x/u_x, \Delta z/u_z)$, where the minimum is taken over every grid point in the domain and $\Delta x, \Delta z$ are the grid spacings in the x and z directions respectively.

The physics of our simulation is fixed by six parameters: L_x, L_z , and k_{0x}, ω_0, F, ν . We describe our choices for these parameters below:

- L_z : Since the wave amplitude grows $\sim e^{z/2H}$, we choose $L_z = 10H$ to give $\sim e^4$ amplitude growth between the damping zones.
- L_x : We want similar grid spacing $\frac{L_x}{N_x} \sim \frac{L_z}{N_z}$. For computational savings, we fix $N_z = 4N_x$. Expecting wave breaking to be mostly in the z direction, we use $L_x = 4H$.
- k_{0x} : Astrophysical IGWs in stars are generally excited by the $l = 2$ component of the tidal potential, for which $k_\perp \sim \frac{1}{R}$ where R is the radius of the star. To best emulate this, we use $k_{0x} = \frac{2\pi}{L_x}$ the smallest permitted wavenumber permitted by periodic boundary conditions.

- ω_0 : We choose ω_0 by evaluating dispersion relation $\omega(k_{0x}, k_{0z})$ for some desired k_{0z} .

Astrophysical IGWs also generally satisfy $\omega \ll N$, or equivalently $\frac{k_r}{k_\perp} \sim k_r R \gg 1$. Since $H \lesssim R$, we aim to study $k_{0z} H \gg 1$. However, to satisfy this well is computationally expensive: $L_z \gg H$ is required to give waves ample room to grow within the simulation domain, but we want k_{0z} to be sufficiently separated from the grid spacing $\sim L_z/N_z$ that nonlinear effects can be seen in later simulations (see subsection 5.2). Thus, N_z sets how well we can satisfy $k_{0z} H \gg 1$; we choose $k_{0z} H = 1$.

- F : We first choose F forcing strength such that $\vec{\xi} \cdot \vec{k} \ll 1$ is satisfied everywhere throughout the domain. This becomes a constraint on F by using Equation 11 and $|\vec{u}| \propto e^{z/2H}$.

- ν : Nonlinear effects transfer wave energy from k_0 to smaller scales. Since well-resolved simulations using spectral methods have no inherent numerical viscosity, energy will accumulate at grid scales in the absence of artificial dissipation. We introduce dissipation parameter ν used for both artificial viscosity and artificial diffusivity. We ensure our equations of motion continue to conserve horizontal momentum (see Section A for details). Under weak forcing, we may set $\nu = 0$, since the energy cascade is negligible.

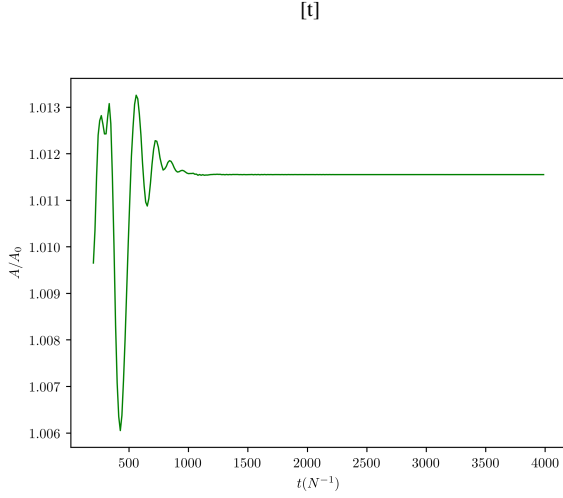


Figure 1. Amplitude of excited wave over time in weak forcing simulation, in units of the analytical estimate Equation 11. We observe great agreement with the linear calculation.

4.2 Damping Layers

To imitate an infinite fluid using a finite simulation domain, we use periodic boundary conditions in the x direction and damping layers at the top and bottom of the z direction. This damps waves that reach the edge of the simulation domain without inducing nonphysical reflection. Specifically, these are implemented by introducing linear damping terms to Equation 2:

$$\begin{aligned} \frac{D\Upsilon}{Dt} + u_z \frac{\partial \ln \rho_0}{\partial z} &= -\Gamma(z)\Upsilon, \\ \frac{D\vec{u}}{Dt} + \vec{\nabla}P + P\vec{\nabla}\Upsilon + g\hat{z} &= -\Gamma(z)\vec{u}, \\ \frac{1}{2\tau} \left[2 + \tanh \frac{z - z_T}{\Delta z} + \tanh \frac{z_B - z}{\Delta z} \right] &= \Gamma(z), \end{aligned} \quad (14)$$

where $z_B = 0.05L_z$, $z_T = 0.95L_z$ are the boundaries of the damping zone. This strongly damps perturbations below z_B and above z_T with damping time τ , negligibly affects dynamics between z_B , z_T and has transition width governed by Δz ; we use $\Delta z = 0.025L_z$. This prescription, used in similar studies (Lecoanet et al. 2016), has the advantage of being smooth, important for spectral methods. The full implementation of the fluid equations in Dedalus is described in Section A.

4.3 Simulation Results

We present the results of a simulation satisfying the parameter choices in subsection 4.1 such that $\vec{\xi} \cdot \vec{k} \ll 1$ everywhere.

5 INTERNAL GRAVITY WAVES: NONLINEAR SIMULATION

5.1 Mean Flow Critical Layer Absorption

A Navier-Stokes numerical viscosity ν is used to damp high wavenumbers and regularize the nonlinear cascade at near grid resolution: $\nu \sim 0.1 \frac{\omega_0}{|k_{0z}|} \frac{L_z}{2\pi N_z}$ was found to be suitable for $N_z = 2048$.

In past studies of IGWs in WDs (cite Fuller & Lai), $\xi_z \equiv \frac{u_z}{\omega_0}$ the

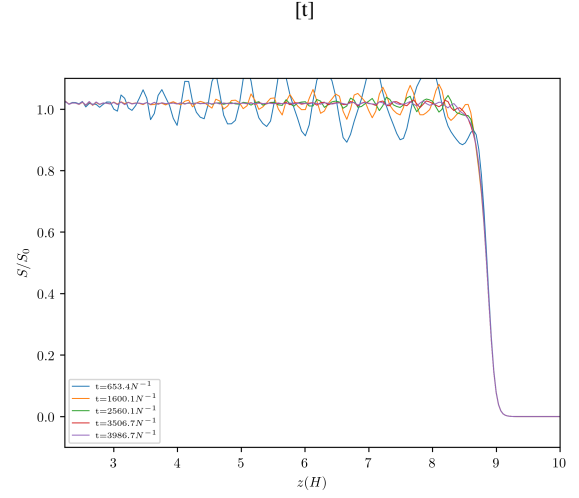


Figure 2. Horizontal momentum flux $S(z, t)$ in units of the analytical estimator given by Equation 9 as a function of z at select times t . As initial transients die out, the flux converges to be flat below the damping layer. The flux excited in the forcing zone is transported without loss to the top of the domain, where it is dissipated by the damping layer (see subsection 4.2) without reflection.

Lagrangian fluid displacement was often used towards wave breaking criterion $k_{0z}\xi_z \gtrsim 1$. We argue that the wave's self-interaction via its generated mean flow \bar{U}_0 induces total absorption when the mean flow exceeds critical value

$$\bar{U}_c = \frac{\omega_0}{k_{0x}}. \quad (15)$$

This is consistent with the picture put forth in e.g. Goldreich and Nicholson (cite).

A purely horizontal shear flow $\bar{U}_0(z)\hat{x}$ can be seen in Equation 1 to have the effect of modifying time derivatives ∂_t to their frequency in the comoving frame of the fluid $\partial_t - \bar{U}_0(z)\partial_x$. For a critical value $\omega_0 - \bar{U}_c k_{0x} = 0$, the frequency of the linear wave in the fluid's frame of reference vanishes and critical behavior is observed. In a linear theory or a theory where small scales are viscosity rather than advection dominated, the incident wave has amplitude reflection and transmission coefficients

$$\mathcal{R} = e^{-2\pi\sqrt{\text{Ri} - \frac{1}{4}}}, \quad \mathcal{T} = e^{-\pi\sqrt{\text{Ri} - \frac{1}{4}}}, \quad (16)$$

where we have defined Richardson number $\text{Ri} \equiv \frac{N^2}{\left(\frac{\partial \bar{U}_0}{\partial z}\right)^2} \Big|_{z_c}$ at the

critical layer z_c : $\bar{U}_0(z_c) = \frac{\omega_0}{k_{0x}}$. For most shear flows, $\text{Ri} \gg 1$ and so $\mathcal{R}, \mathcal{T} \ll 1$ and the incident wave is absorbed.

When the fluid absorbs the incident wave, it absorbs the incident horizontal momentum flux as well, which is converted into additional horizontal momentum of the shear flow. Since the shear flow cannot exceed \bar{U}_c the horizontal phase velocity of the incident wave, the critical layer must thus propagate downwards (towards the wave source) to accommodate the incident momentum. In other words, the total horizontal momentum of the shear flow obeys conservation equation

$$\frac{\partial}{\partial t} \int_0^{L_z} \rho(z) \bar{U}_0(z, t) dz - \Delta S = 0. \quad (17)$$

We define ΔS to be the change in flux across the critical layer, or equivalently the absorbed flux. Treating $\bar{U}_0(z > z_c) = \bar{U}_c, \bar{U}(z < z_c) = 0$ gives us exactly

$$\rho \bar{U}_c \frac{\partial z_c}{\partial t} = -\Delta S. \quad (18)$$

For constant ΔS in space and $\rho \approx \rho_0$, this has analytical solution

$$z(t) = -H \ln t - H \ln \frac{H \rho_0(z=0) c_{ph,x}}{\Delta S}. \quad (19)$$

5.2 Numerical Simulation

We use the same k_{0x}, ω_0 as subsection 4.3. Our other parameters are:

- We choose $\nu = 0.1 \frac{\omega_0}{k_{0z} k_{z,\max}}$, where $k_{z,\max} = \frac{2\pi N_z}{L_z}$. Note that $\nu = \frac{\omega_0}{k_{0z} k_{z,\max}}$ corresponds to the advective term $\vec{u} \cdot \vec{\nabla}$ being of the same order as the time derivative ∂_t for flow velocities $\vec{u} \sim \frac{\omega_0}{k_{0z}}$ at the grid spacing.

Two representative snapshots from our simulation are provided in TODO after the critical layer has had time to form. We may note that the critical layer, where S_{px} is absorbed and $\bar{U}_0 = \bar{U}_c$, travels downwards as predicted.

5.3 Propagating Critical Layer

For the simulation in TODO, we may define $z_c = \arg\max_z \frac{\partial \bar{U}_0}{\partial z}$. Computing $\frac{\partial z_c}{\partial t}$ using the analytical flux Equation 9 allows comparison to Equation 18, which we exhibit in TODO. We see overall good agreement, though some small deviation is expected since S_{px} is not perfectly conserved owing to numerical viscosity (and YUBONOTE S_{px} is misestimated?).

However, recalling Equation 16, we only expect complete critical layer absorption when $Ri \gg \frac{1}{4}$. We may plot Ri over the same time interval in TODO. We may observe that the Richardson number is initially decreasing but eventually levels out and begins to increase again. This corresponds to an increasingly sharp critical layer transition then subsequently a decreasingly sharp critical layer transition.

We argue that the Richardson number is bounded from below by viscosity. A repeated simulation with a larger viscosity is shown in TODO, where the Richardson number does not go nearly as low.

6 DISCUSSION

6.1 Applicability to Astrophysical Systems

Discussion foo

7 ACKNOWLEDGEMENTS

REFERENCES

- Andrews D., McIntyre M. E., 1976, Journal of the Atmospheric Sciences, 33, 2031
 Ascher U. M., Ruuth S. J., Spiteri R. J., 1997, Applied Numerical Mathematics, 25, 151
 Barker A. J., Ogilvie G. I., 2010, MNRAS, 404, 1849
 Booker J. R., Bretherton F. P., 1967, J. Fluid Mech, 27, 513–539
 Boyd J. P., 2001, Chebyshev and Fourier spectral methods. Courier Corporation

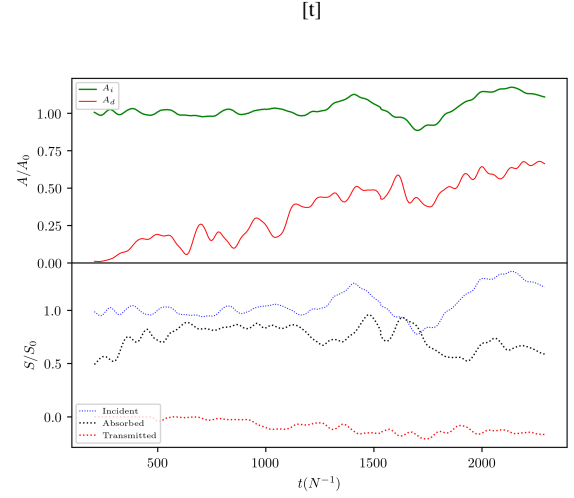


Figure 3. The top panel measures the incident wave amplitude $A_i(t)$ (green) and the downwards propagating wave amplitude $A_d(t)$ (red) just above the forcing zone, normalized to the analytical estimate Equation 11. $A_d \neq 0$ due to reflection off the critical layer. The bottom panel shows the behavior of three horizontal momentum fluxes over time, in units of the analytical estimate Equation 9: (blue) flux incident on the critical layer, (black) flux absorbed by the critical layer, and (green) flux transmitted through the critical layer. A fiducial simulation of $Re = 1000$ is shown.

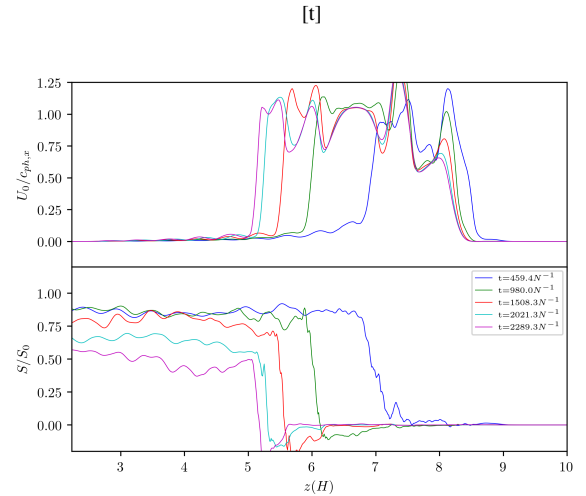


Figure 4. The top and bottom panels show respectively the mean flow \bar{U}_0 (see Equation 13) and horizontal momentum flux S (see Equation 8) as a function of z at certain times t . The same color coding is used for the two plots. The mean flow is normalized to its critical value $c_{ph,x}$ while again S is normalized to its analytical estimate Equation 9.

- Brown S., Stewartson K., 1982, Journal of Fluid Mechanics, 115, 217
 Burns K. J., Vasil G. M., Oishi J. S., Lecoanet D., Brown B., 2016, Dedalus: Flexible framework for spectrally solving differential equations, Astrophysics Source Code Library (ascl:1603.015)
 Dosser H. V., Sutherland B. R., 2011a, J. Atmos. Chem., 68, 2844
 Dosser H., Sutherland B., 2011b, Physica D: Nonlinear Phenomena, 240, 346
 Drazin P., 1977, Proc. R. Soc. Lond. A, 356, 411
 Fuller J., Lai D., 2011, MNRAS, 412, 1331
 Fuller J., Lai D., 2012a, MNRAS, 421, 426

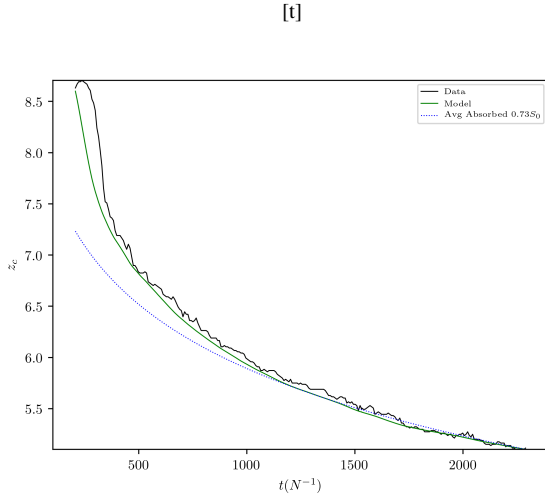


Figure 5. Shown is the position of the critical layer (black) as well as two predictors of the critical layer location using the absorbed flux (see the second panel of Figure 3). The green line is generated by integrating Equation 18 using ΔS from the data, while the blue line is generated by using the average value of ΔS in Equation 19.

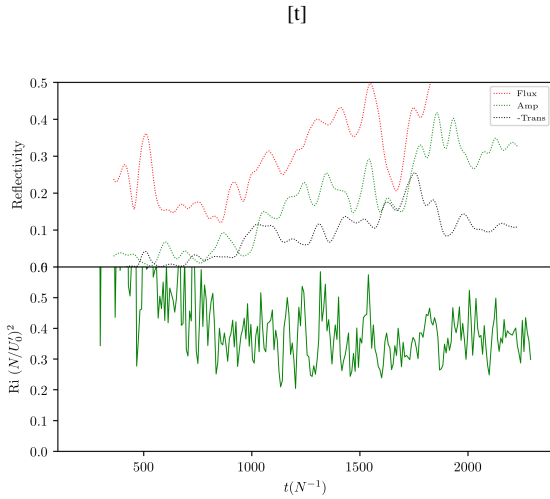


Figure 6. NL reflectivity

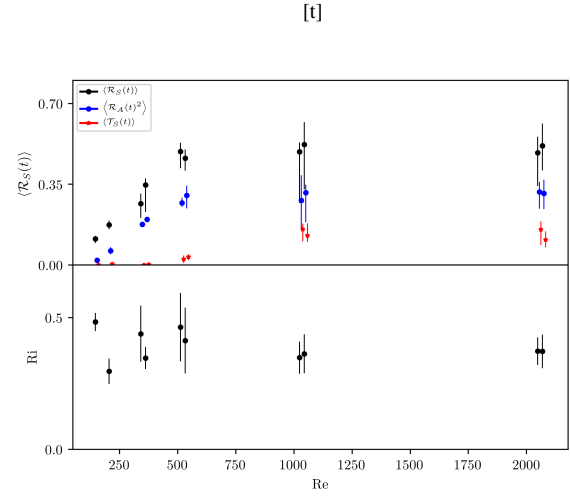


Figure 7. Convergence w/ all runs

- Maoz D., Sharon K., Gal-Yam A., 2010, *ApJ*, 722, 1879
 Nelemans G., 2009, *Class. Quantum Grav*, 26, 094030
 Perets H. B., et al., 2010, *Nature*, 465, 322
 Shen K. J., et al., 2018, *AJ*, 865, 15
 Webbink R., 1984, *ApJ*, 277, 355
 Winters K. B., D'Asaro E. A., 1994, *J. Fluid Mech*, 272, 255–284
 Zahn J.-P., 1975, *A&A*, 41, 329

- Fuller J., Lai D., 2012b, *ApJL*, 756, L17
 Fuller J., Lai D., 2013, *MNRAS*, 430, 274
 García-Berro E., Badenes C., Aznar-Siguán G., Lorén-Aguilar P., 2017, *MNRAS*, 468, 4815
 Gilfanov M., Bogdán Á., 2010, *Nature*, 463, 924
 Goldreich P., Nicholson P. D., 1989, *ApJ*, 342, 1079
 Hazel P., 1967, *J. Fluid Mech*, 30, 775–783
 Iben Jr I., Tutukov A. V., 1984, *ApJS*, 54, 335
 Kilic M., Hambly N. C., Bergeron P., Genest-Beaulieu C., Rowell N., 2018, *MNRAS*, 479, L113
 Klostermeyer J., 1991, *Geophysical & Astrophysical Fluid Dynamics*, 61, 1
 Korol V., Rossi E. M., Groot P. J., Nelemans G., Toonen S., Brown A. G. A., 2017, *MNRAS*, 470, 1894
 Lecoanet D., Vasil G. M., Fuller J., Cantiello M., Burns K. J., 2016, *Monthly Notices of the Royal Astronomical Society*, 466, 2181
 Lindzen R. S., Holton J. R., 1968, *Journal of the Atmospheric Sciences*, 25, 1095

APPENDIX A: EQUATION IMPLEMENTATIONS

We denote $x \in [0, L_x], z \in [0, L_z]$ the simulation domain and N_x, N_z the number of spectral modes in the respective dimensions. We perform direct numerical simulation of Equation 10 with the open-source pseudo-spectral code Dedalus (CITE).

Numerically, the nonlinear $\frac{\vec{\nabla} P}{\rho}$ term is problematic: we desire a system where the fluid fields are not divided by one another. We introduce $\varpi = \frac{P}{\rho}$ instead, then mandate ρ_0, ϖ_0 background fields satisfy hydrostatic equilibrium $\vec{\nabla} \varpi_0 + \varpi_0 \vec{\nabla} \rho_0 + g \hat{z} = 0$. Taking isothermal stratification, we find $\varpi_0 = gH$. We further change variables to $\Upsilon = \ln \rho - \ln \rho_0$ and $\varpi_1 = \varpi - \varpi_0$ deviations from the background state to obtain a system of equations at most quadratic in fluid fields:

$$\vec{\nabla} \cdot \vec{u} = 0, \quad (\text{A1a})$$

$$\frac{\partial \Upsilon}{\partial t} + (\vec{u} \cdot \vec{\nabla}) \Upsilon - \frac{u_z}{H} = 0, \quad (\text{A1b})$$

$$\frac{\partial u_x}{\partial t} + (\vec{u} \cdot \vec{\nabla}) u_x + \frac{\partial \varpi_1}{\partial x} + gH \frac{\partial \Upsilon}{\partial x} + \varpi_1 \frac{\partial \Upsilon}{\partial x} = 0, \quad (\text{A1c})$$

$$\frac{\partial u_z}{\partial t} + (\vec{u} \cdot \vec{\nabla}) u_z + \frac{\partial \varpi_1}{\partial z} + gH \frac{\partial \Upsilon}{\partial z} + \varpi_1 \frac{\partial \Upsilon}{\partial z} - \frac{\varpi_1}{H} = 0. \quad (\text{A1d})$$

It bears noting that these equations are exactly equivalent to the original Euler equations and hence conserve horizontal momentum.

A1 Artificial Dissipation

The nonlinear terms in the above equations will transfer energy from lower wavenumbers to higher wavenumbers. Since spectral codes have no numerical dissipation, artificial dissipation must be added. To ensure the dissipative system conserves horizontal momentum, we begin by adding dissipative terms to the flux-conservative form of the Euler fluid equations Equation 1 (we use stress tensor $\tau_{ij} = P\delta_{ij}$):

$$\vec{\nabla} \cdot \vec{u} = 0, \quad (\text{A2a})$$

$$\partial_t \rho + \vec{\nabla} \cdot (\rho \vec{u} - \nu \vec{\nabla}(\rho - \rho_0)) = 0, \quad (\text{A2b})$$

$$\partial_t (\rho \vec{u}) + \vec{\nabla} \cdot (\rho \vec{u} \vec{u} + \text{diag}(\rho \varpi) - \nu \rho \vec{\nabla} \vec{u}) + \rho g \hat{z} = 0. \quad (\text{A2c})$$

The same ν is used for both the diffusive and viscous term, though this is not required. Since the dissipation is not physical and is purely used for numerical stability, we choose it such that hydrostatic equilibrium is not modified. Some algebraic manipulation to re-cast it in the form of Equation A1 gives

$$\vec{\nabla} \cdot \vec{u} = 0, \quad (\text{A3a})$$

$$\partial_t \Upsilon + (\vec{u} \cdot \vec{\nabla}) \Upsilon - \frac{u_z}{H} - \nu \left(\nabla^2 \Upsilon + (\vec{\nabla} \Upsilon) \cdot (\vec{\nabla} \Upsilon) - \frac{2}{H} \partial_z \Upsilon + \frac{1 - e^{-\Upsilon}}{H^2} \right) = 0, \quad (\text{A3b})$$

$$\begin{aligned} \partial_t \vec{u} + (\vec{u} \cdot \vec{\nabla}) \vec{u} + \vec{\nabla} \varpi + \varpi \vec{\nabla} \Upsilon - \nu \nabla^2 \vec{u} + \vec{u} \nu \left(\nabla^2 \Upsilon + (\vec{\nabla} \Upsilon) \cdot (\vec{\nabla} \Upsilon) - \frac{2}{H} \partial_z \Upsilon + \frac{1 - e^{-\Upsilon}}{H^2} \right) \\ - 2\nu \left(((\vec{\nabla} \Upsilon) \cdot \vec{\nabla}) \vec{u} - \frac{1}{H} \partial_z \vec{u} \right) - \frac{\varpi_1}{H} = 0. \end{aligned} \quad (\text{A3c})$$

Hydrostatic equilibrium is still $\vec{\nabla} \varpi_0 + g \hat{z} = 0$ where $\rho = \rho_0, \vec{u} = 0$. Including the damping layers and forcing terms as described in subsection 4.1, we finally obtain the full system of equations as simulated in Dedalus:

$$\vec{\nabla} \cdot \vec{u} = 0, \quad (\text{A4a})$$

$$\begin{aligned} \partial_t \Upsilon - \frac{u_z}{H} = \nu \left(\nabla^2 \Upsilon + (\vec{\nabla} \Upsilon) \cdot (\vec{\nabla} \Upsilon) - \frac{2}{H} \partial_z \Upsilon + \frac{1 - e^{-\Upsilon}}{H^2} \right), \\ - (\vec{u} \cdot \vec{\nabla}) \Upsilon - \Gamma(z) \Upsilon + \frac{F}{\rho_0(z)} e^{-\frac{(z-z_0)^2}{2\sigma^2}} \cos(k_x x - \omega t), \end{aligned} \quad (\text{A4b})$$

$$\begin{aligned} \frac{\partial u_x}{\partial t} + \frac{\partial T}{\partial x} + gH \frac{\partial \Upsilon}{\partial x} = \nu \nabla^2 u_x - u_x \nu \left(\nabla^2 \Upsilon + (\vec{\nabla} \Upsilon) \cdot (\vec{\nabla} \Upsilon) - \frac{2}{H} \partial_z \Upsilon + \frac{1 - e^{-\Upsilon}}{H^2} \right) \\ + 2\nu \left(((\vec{\nabla} \Upsilon) \cdot \vec{\nabla}) u_x - \frac{1}{H} \partial_z u_x \right) - \Gamma(z) u_x - (\vec{u} \cdot \vec{\nabla}) u_x - T_1 \frac{\partial \Upsilon}{\partial x}, \end{aligned} \quad (\text{A4c})$$

$$\begin{aligned} \frac{\partial u_z}{\partial t} + \frac{\partial T}{\partial z} + gH \frac{\partial \Upsilon}{\partial z} - \frac{T_1}{H} = \nu \nabla^2 u_z - u_z \nu \left(\nabla^2 \Upsilon + (\vec{\nabla} \Upsilon) \cdot (\vec{\nabla} \Upsilon) - \frac{2}{H} \partial_z \Upsilon + \frac{1 - e^{-\Upsilon}}{H^2} \right) \\ + 2\nu \left(((\vec{\nabla} \Upsilon) \cdot \vec{\nabla}) u_z - \frac{1}{H} \partial_z u_z \right) - \Gamma(z) u_z - (\vec{u} \cdot \vec{\nabla}) u_z - T_1 \frac{\partial \Upsilon}{\partial z}. \end{aligned} \quad (\text{A4d})$$